Macromolecules
ARTICLE
pubs.acs.org/Macromolecules

Liquidlike Poly(ethylene glycol) Supported in the Organic−Inorganic Matrix for CO_2 Removal

Jianzhong Xia,[†,‡] Songlin Liu,[‡] Cher Hon Lau,[‡] and Tai-Shung Chung*[,‡]

[†]NUS Graduate School for Integrative Sciences and Engineering, National University of Singapore, 28 Medical Drive, Singapore 117456, Singapore

[‡]Department of Chemical and Biomolecular Engineering, National University of Singapore, 10 Kent Ridge Crescent, Singapore 119260, Singapore

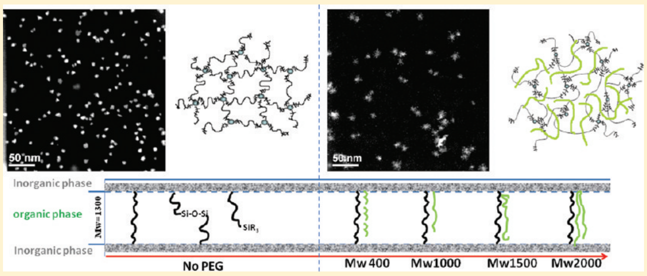

ABSTRACT: This paper introduces a novel method to improve CO_2 permeability and CO_2/light gas permselectivity by adding poly(ethylene glycol) (PEG) into the PEG−silica organic−inorganic hybrid matrix. The matrix is cross-linked by in-situ formation of silica nanoparticles with diameters ranging from 1 to 5 nm. These particles disperse homogenously in the organic phase according to the morphology studied by scanning TEM. Much small particles were evolved after blending PEG into the matrix due to more fraction of bifunctional and trifunctional silicon containing groups. Four PEGs with different molecular weights (M_w = 400, 1000, 1500, and 2000 g/mol) are added into the matrix prior to the matrix formation. Permeability coefficients of three pure gases (H_2, N_2, and CO_2) and one mixed gas (CO_2/N_2) are measured to explore the effects of PEG content and molecular weight on the gas transport properties. The membrane containing 60 wt % of 1000 g/mol PEG could achieve an ultrahigh CO_2 permeability of 845 barrer with CO_2/H_2 and CO_2/N_2 permselectivity around 10 and 40, respectively. Fundamental studies on the effect of temperature on gas diffusivity and solubility are also carried out. Molecular weights of PEGs have been proved to play a crucial role in determining the permeability and diffusivity.

INTRODUCTION

The failure of 2010 United Nations Climate Change Conference in Cancun clearly indicated the increasing difficulty in forcing governments around the world to control carbon dioxide emission.[1] In this context, technology of clean energy generation emerges as an important solution to overcome the dilemma between the economic development and the fight against global warming.[2] Reports show that more than 30% of CO_2 produced by human activities are attributed to the running of coal-fired power stations.[3] In this sense, the capture of CO_2 in the coal-fired power generation industry is especially significant in worldwide CO_2 control. Meanwhile, compared with other small individual sources of CO_2 emission, large and centralized coal-fired power stations provide more convenience in the monitoring and control of CO_2. Therefore, the technology for CO_2 removal from large coal-fired power plants is highly demanded.

The IGCC (Integrated Gasification Combined Cycle) power plant program, which is the core technology of FutureGen sponsored by U.S. Department of Energy, requires extensive applications of highly efficient CO_2 removal technology.[4] Currently, there are three major approaches to reduce CO_2 emission: precombustion capture, oxyfuel combustion, and postcombustion capture.[5] In the typical precombustion capture process of the IGCC power plants, the coal slurry is fed into a gasifier with enriched oxygen and water steam to generate hydrogen and carbon monoxide. The gas mixtures are then routed into a WGS (water gas shift) reactor to produce more hydrogen by reacting CO with water vapor. The details of these reactions are as follows:

$$3C\ (\text{i.e., coal}) + O_2 + H_2O \rightarrow 3CO + H_2 \qquad (1)$$

$$CO + H_2O \rightarrow CO_2 + H_2 \qquad (2)$$

Before the stream flows into the H_2 gas turbine, a CO_2 separation technology is needed to effectively remove CO_2. This CO_2 separation technology also has great potential in postcombustion CO_2 capture, which involves direct CO_2 removal from flue gas consisting of CO_2, N_2, and H_2O. Several technologies have been developed for CO_2 separation from light gases, including amine adsorption,[6] pressure-swing adsorption,[7] and membrane separation.[4,8−18] Each technology has its own pros and cons. Membrane separation systems have drawbacks at the current stage, such as relatively lower permselectivity for CO_2 over light gases and additional recompression cost compared to amine-based adsorption systems; however, membrane-based CO_2 capture business appears to be promising because new materials with ultrahigh CO_2 permeability or permeance have been continuously developed.[5]

Conventional gas separation membranes made from glassy polymers are mainly based on the size-sieving mechanism. For example, H_2-selective glassy membranes work because H_2 gas molecules are

Received: April 20, 2011
Revised: May 26, 2011
Published: June 15, 2011

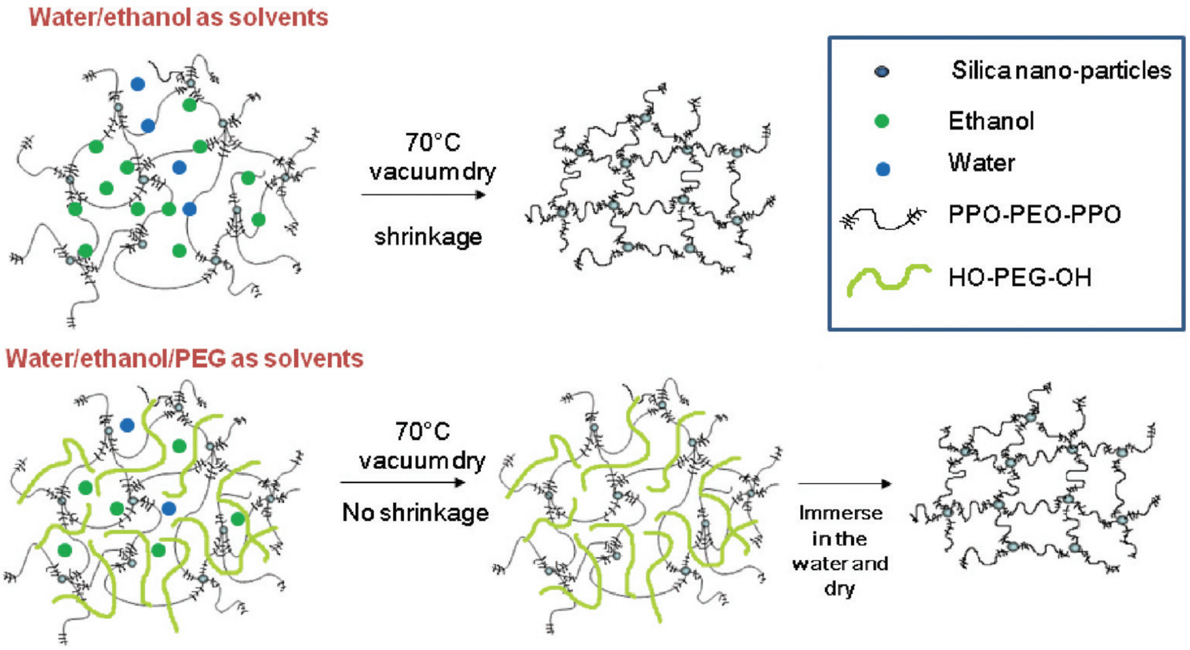

Figure 1. Concept of liquid PEGs supported in the organic−inorganic matrix.

smaller and thus penetrate faster than CO_2.[19−21] Compared with rubbery membranes, glassy membranes have better thermal stability and mechanical property.[22] However, most glassy membranes have a relatively lower CO_2 permeability than rubbery membranes. Moreover, as there is a trade-off relation between gas permeability and permselectivity, glassy membranes are further inferior to rubbery membranes for CO_2 removal.[23] Reverse-selective membranes made from rubbery materials, like silicon rubber[24,25] and poly(ethylene oxide) (PEO),[15,26−36] could be promising materials for CO_2 removal because larger CO_2 molecules, due to higher solubility, can pass through these membranes faster than H_2 and N_2. In recent years, many PEO- or poly(ethylene glycol) (PEG)-based CO_2 reversible selective membranes have been developed because of their high ether oxygen concentrations, including PEO copolymers,[16,30,37] PEO blends,[8,9,30,33,34,37−40] and cross-linked PEO.[11,15,33,41−44] However, PEO are easy to crystallize, resulting in reduced free volume and lower permeability.[28]

Many approaches have been reported to reduce the crystallization tendency of PEO/PEG. They may be briefly summarized as follows based on their own unique systems.

(a) PEO copolymer: The crystallization of ethylene oxide (EO) segments could be prevented if the EO segments are too short to line up with the neighboring EO chains.[39]

(b) Cross-linked PEO: Lin et al.[15,26] have developed a series of membranes that CO_2 permeability could reach 400 barrer at 35 °C by cross-linking poly(ethylene glycol diacrylate).[26] Shao and Chung[10] have synthesized a series of cross-linked organic−inorganic membranes by in-situ formation of silica nanoparticles. The CO_2 permeability of these membranes could reach 300−492 barrer with ideal permselectivity of 8−9.

(c) PEO blends: Liquid PEG (M_w = 300 g/mol) was directly impregnated into the microporous region of a cellulose membranes by Kawakami et al.[40] Surprisingly, CO_2 permeability was only 82 barrer at 25 °C due to the microporous tortuosity and the less permeable cellulose substrate. In order to further improve CO_2 permeability and permselectivity, Car et al.[34,37,38] and Yave et al.[8,9,30] have incorporated liquid PEG into thermoplastic poly(amide-*b*-ethylene oxide) and poly(ethylene oxide)−poly(butylene terephthalate) multiblock copolymers via physical blending. However, the high percentage of hard amide segments in these copolymers still has a negative effect on permeability enhancement.

Ideally, liquid PEG should be the best selective medium for CO_2 removal because of its high solubility and diffusivity as well as the high permselectivity of CO_2/light gas. However, liquid PEG itself cannot form a free-standing membrane. Thus, a proper selection of matrix materials for hosting PEG is the key factor to effectively use its superior gas separation properties toward the separation of CO_2/light gas.

In this study, the organic−inorganic system developed in our previous work[10] is employed as the matrix to support the liquid PEG. In-situ-formed silica nanoparticles connect the poly(propylene oxide)-*b*-poly(ethylene oxide)-*b*-poly(propylene oxide) (PPO−PEO−PPO) chains, thus forming a dense membrane with enough mechanical strength. Low molecular weight PEGs (M_w = 400, 1000, 1500, and 2000 g/mol) are directly blended in the matrix as shown in Figure 1. This technique has a few advantages: (1) high capacity to host free PEGs (up to 60 wt %); (2) similar structure between the matrix and the free PEGs; (3) permeability could be tailored by changing the content or the molecular weight of the PEGs. CO_2 permeability ranging from 55.6 to 1040 barrer is achieved by using different PEGs at temperatures from 35 to 55 °C. CO_2/H_2 and CO_2/N_2 permselectivity varies from 6.0 to 10.7 and 26.2 to 52.4, respectively. The effect of temperature is so significant that the permeability will increase 15 times with a temperature increment by 25 °C. The elimination of PEG crystals is the major reason for the permeability jump. CO_2 sorption study reveals that CO_2 solubility increases when the PEG melts. Among all these PEGs, PEG1000 is found to be the best candidate to maximize both permeability and permselectivity. Interestingly, CO_2 diffuses faster if the molecular weight of PEGs is comparable with PEO segments in the matrix.

Scheme 1. Synthetic Route of Hybrid Membranes

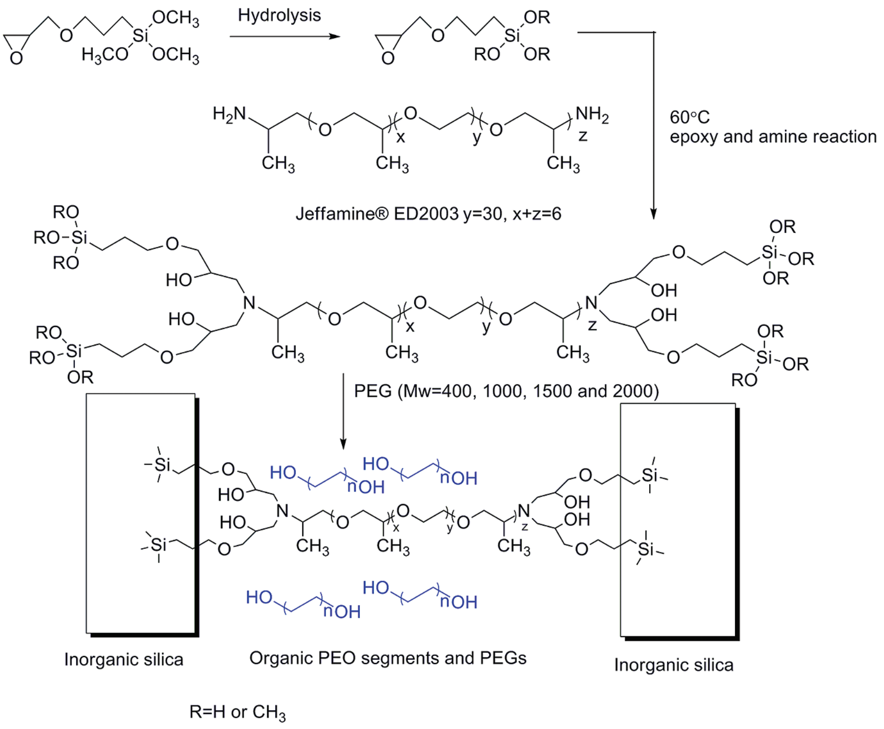

BACKGROUND

1. Permeability and Sorption. The solution-diffusion mechanism is applied to explain the gas transport phenomena for this study. The permeability (P) may be expressed as the product of diffusivity (D) and solubility (S).

$$P = DS \tag{3}$$

The ideal selectivity of membranes for pure gases A and B is defined as follows:

$$\alpha_{A,B} = \frac{P_A}{P_B} = \frac{D_A S_A}{D_B S_B} \tag{4}$$

The actual gas solubility can be obtained by directly measuring the weight gain of the sample under increasing pressure of one particular gas. Henry sorption, as often observed in liquids and rubbery polymers, may be illustrated using the same equation as in liquids:

$$C_D(p) = k_D p \tag{5}$$

where $C_D(p)$ is the gas concentration in the polymer at pressure p and k_D is the Henry constant.

2. Effect of Temperature. The temperature dependence of solubility, diffusivity, and permeability coefficients may be described by a van't Hoff expression and two Arrhenius expressions, respectively, with the absence of thermal transitions.[45,46]

$$S = S_0 \exp(-H_s/RT) \tag{6}$$

$$D = D_0 \exp(-E_d/RT) \tag{7}$$

$$P = P_0 \exp(-E_p/RT) \tag{8}$$

where S_0, D_0, and P_0 are the pre-exponential factors. H_s is the heat of sorption, E_d is the activation energy for diffusion, and E_p is the apparent activation energy for permeation. Because the sorption could be considered as the marriage of two hypothetical thermodynamic steps, which are the condensation of the pure penetrant and the mixing of the pure penetrant with the polymer matrix, the apparent activation energy could be rewritten as follows:

$$E_p = E_d + \Delta H_{cond} + \Delta H_{mix} \tag{9}$$

EXPERIMENTAL SECTION

1. Materials and Membrane Preparation. Jaffamine ED-2003 (O,O'-bis(2-aminopropyl)polypropylene glycol-*block*-poly(ethylene glycol)-*block*-polypropylene glycol, molecular weight: 2000 g/mol), ethanol (AR grade), 3-glycidyloxypropyltrimethoxysilane (GOTMS), and poly(ethylene glycol) (400, 1000, 1500, and 2000 g/mol) were purchased from Sigma-Aldrich. Concentrated hydrochloric acid from Fisher Scientific was employed as the catalyst for the hydrolysis of GOTMS.

The synthetic route as shown in Scheme 1 is similar to the report in Shao and Chung's work.[10] The molar ratio of GOTMS, ethanol, water, and hydrochloric acid in the hydrolysis solution was 1:1.13:3.2:0.05. After stirring for 60 min at room temperature, the alkoxysilane solution was transferred to the mixed solvent of water/ethanol (30/70 wt %) containing 2 wt % of Jaffamine ED-2003. The molar ratio of GOTMS to Jaffamine ED-2003 was kept at 4:1 in all samples. The solution was then heated up to 60 °C and kept stirring for 1 h to facilitate the epoxy—amine reaction and preliminary condensation. Afterward, the predetermined amount of PEG was added into the mixture and stirred for 10 min, followed by filtration with 5 μm Waterman filter. The solution was poured into a homemade Teflon Petri dish which was already placed levelly in the oven at 30 °C. The Teflon dish was covered with an aluminum foil with small holes to control the evaporation rate of solvent.

After drying at 30 °C for 1 day, the oven temperature was increased to 40 °C for 2 days. Subsequently, the membranes were moved into a vacuum oven at 70 °C for 1 day to complete the condensation reaction and remove the residual solvents. The membranes were sealed into a zip bag and put into a refrigerator (−20 °C) for 2 h to induce crystallization of the free PEGs which were dispersed in the GOTMS−Jaffamine matrix. At the end, the membrane samples were peeled off from Petri dish and stored in a desiccator for testing and characterizations. The thermal history of these samples was kept the same for easy comparison of various properties.

The molar ratio of GOTMS to Jaffamine ED-2003 was maintained at 4:1 for all the matrices. The gas permeation performance of the hybrid membranes in other ratios could be found in the previous work.[10] Four PEGs (all with two hydroxyl end groups) of different molecular weights were blended into the GOTMS−PEO (also referred as GP w/o PEG) matrices. The blended hybrid membranes are represented by GPP*X*-*Y*-*Z*, in which GPP represents the GOTMS−PEO−PEG blend, *X* represents the molecular weight of blended PEG, *Y* represents the weight percentage of the blended PEG, and *Z* represents the temperature. For example, GPP1000-40-35 means the matrix contains 40 wt % of free PEG1000 tested at 35 °C.

2. Gel Content. To examine the extent of polycondensation in this sol−gel system, the nascent membranes were subjected to water immersion for 1 week. The remaining insoluble samples were dried in the vacuum at 70 °C for 24 h to remove water before weighing again. The gel content was calculated by eq 10.

$$\% \text{ gel content} = m/m_0 \times 100\% \qquad (10)$$

where m and m_0 are the weights of the insoluble fraction and the original weight of the membrane, respectively.

3. Measurements of Gas Permeation Properties. The pure gas permeability coefficients were determined by the constant volume method. Detailed experimental design and procedure could be found elsewhere.[47] The permeability at 2 atm for all the membranes was collected by the order of N_2, H_2, and CO_2 at 35 and 45 °C.

The mixed gas permeation properties for these hybrid membranes were obtained with a homemade mixed gas permeation cell as described in the work of Li et al.[48] GPP1000-60 and GPP1500-60 were selected for mixed gas permeation tests because of their good pure gas permeation performance. Samples were tested with a CO_2/N_2 (50%/50% mole fraction) binary gas at 45 °C with a total pressure of 4 atm.

4. Measurements of Gas Sorption. CO_2 sorption measurements for all the samples at 35 and 45 °C were made by using the gravimetric sorption technique (Cahn D200 microbalance sorption cell). The sorption cell with sample was evacuated overnight to eliminate the residual solvents and absorbed gases. Details about the testing procedure could be found elsewhere.[49] From the weight gain, the amount of gas absorbed could be calculated after deducting the contribution from the buoyancy. The solubility could be obtained from the slope of the sorption amount versus pressure. The diffusivity of gas penetrants in the membrane was calculated from solubility and permeability according to eq 3.

5. Characterizations. DSC was performed on a DSC822 (Mettler Toledo) from −100 to 100 °C with a heating and cooling rate of 10 °C/min. Ultrathin films for a combined scanning transmission electron microscope (STEM/EDX) were prepared by a solution method following the procedure used for membrane casting. A wide-angle X-ray diffractometer (Bruker D8) was utilized to determine the structures of the membranes at room temperature (25 °C). Ni-filtered Cu Kα radiation with a wavelength of 1.54 Å was used in the XRD experiments. The *d*-spacing was calculated based on the Bragg's law $n\lambda = 2d \sin \theta$, where n is the integral number, λ is the wavelength, d is the dimension spacing, and 2θ is the diffraction angle.

Table 1. Gel Content (%) of GP w/o PEG and GPP Series

GP w/o PEG	96 ± 1		
	20 wt %	40 wt %	60 wt %
GPP400	75 ± 1	53 ± 2	36 ± 2
GPP1000	76 ± 1	56 ± 1	34 ± 1
GPP1500	77 ± 1	55 ± 2	33 ± 2
GPP2000	77 ± 1	58 ± 1	36 ± 2

RESULTS AND DISCUSSION

1. Basic Physicochemical Properties. All the membrane samples show cross-linked characteristics in gel content experiments as summarized in Table 1. For the GP w/o PEG sample, 96% of the reactants are cross-linked. For other samples with blended PEGs, the organic−inorganic matrices are insoluble while the blended PEGs can be completely washed out. On the whole, the organic−inorganic matrix is successfully fabricated regardless of the PEG loading.

The GP w/o PEG and GPP400 membranes are transparent because their melting points are below room temperature as shown in Table 2, while GPP1000, GPP1500, and GPP2000 are translucent due to the existence of PEG crystals. Transparency of GPP400 series indicates that the silica nanoparticles are dispersed homogeneously.

Good dispersion of silica nanoparticles in the matrix is also observed in the STEM graphs given in Figure 2a,b. The EDX spectrum in Figure 2c reveals that these nanoparticles are composed of silica. The regular shape and sharp edges of nanoparticles in Figure 2a show that these particles are in the crystal form. The distance between two particles varies from 5 to 50 nm, most of which are larger than the fully extended PPO−PEO−PPO polymer chain (∼10 nm estimated from the bond length). Thus, incomplete cross-linking may exist. In this sol−gel system, any intermediates species, like $[-Si-(OH)_2OCH_3]$ or $[-Si-(OCH_3)_2OH]$, would be considered as the result of partial hydrolysis and condensation. In addition, two partially hydrolyzed species may link together to form a siloxane [Si−O−Si] bond as illustrated by structure B in Figure 3c. In other words, not all the silicon portion of the precursors will participate in the construction of silica nanoparticles. Instead, some of them may only contribute one silicon-containing group while the rest remains flexible. The white dashed lines in Figure 3a are drawn for the illustration of possible network topology. In Figure 3b, the white solid lines schematically represent the possible polymer alignment. Four kinds of groups with different degrees of hydrolysis (i.e., A, B, C, and D in the bottom of Figure 3c) play different roles in constructing the network. The unhydrolyzed groups (A) prevent the precursor from cross-linking and functions as the end groups as illustrated in Figure 3b. The monofunctional groups (B) bridge two cross-linking precursors and extend the polymer chain length between two nanoparticles. Bifunctional (C) and trifunctional (D) groups may cross-link together and form the silica nanoparticles. The silicon signal of unhydrolyzed (A) and monofunctional (B) groups cannot be observed by STEM due to the resolution limitation.

The above hypotheses are supported by the analyses done by ImageJ[50] as shown in Figure 4a and Table 3. In the image analyses, black and white are inversed for better particles identification. The average particle size (nm^2) and the total area fraction are calculated by using different STEM pictures to achieve statistical results. On the basis of the 2-D area fraction

Table 2. Thermal Properties of GPP Series, GP w/o PEG, and Pure PEGs

	T_{m2o} (°C)[a]	T_{m2p} (°C)[b]	T_{c2o} (°C)[c]	T_{c2p} (°C)[d]	$-\Delta H_c$ (J/g)[e]	$-\Delta H'_c$ (J/g)[f]
GP w/o PEG	14.9	24.5	−20.1	−24.5	51	N/A
Jaffamine ED-2003	29.4	37.2	15.6	11.2	114	N/A
GPP400-20	9.7	20.5	−6.8	−13.8	58	66
GPP400-40	7.2	19.3	−7.7	−14.3	77	80
GPP400-60	6.4	20.0	−5.7	−13.3	88	95
PEG400	−9.5	7.7	−15.1	−21.2	123	N/A
GPP1000-20	−8.1	35.2	12.5	4.5	74	73
GPP1000-40	16	41.7	20.8	14.2	92	94
GPP1000-60	21.6	45.0	24.9	15.7	120	116
PEG1000	32.3	40.7	26.7	22.3	159	N/A
GPP1500-20	32.3	43.3	10.9	1.5	75	73
GPP1500-40	42.2	46.8	22.9	17.3	87	94
GPP1500-60	42.3	48.5	26.7	23.5	115	115
PEG1500	37.7	47.0	24.0	19.5	158	N/A
GPP2000-20	35.8	46.2	15.9	7.2	70	76
GPP2000-40	47.2	52.3	29.3	26.0	102	101
GPP2000-60	51.7	54.7	32.8	28.0	123	125
PEG2000	48.2	56.2	34.3	29.7	175	N/A

[a] Onset melting temperature of the second heating curve. [b] Peak melting temperature of the second heating curve. [c] Onset crystallization temperature of the second cooling curve. [d] Peak crystallization temperature of the second cooling curve. [e] ΔH_c is the heat of crystallization obtained experimentally from DSC. [f] $\Delta H'_c$ is the theoretical value calculated by eq 11.

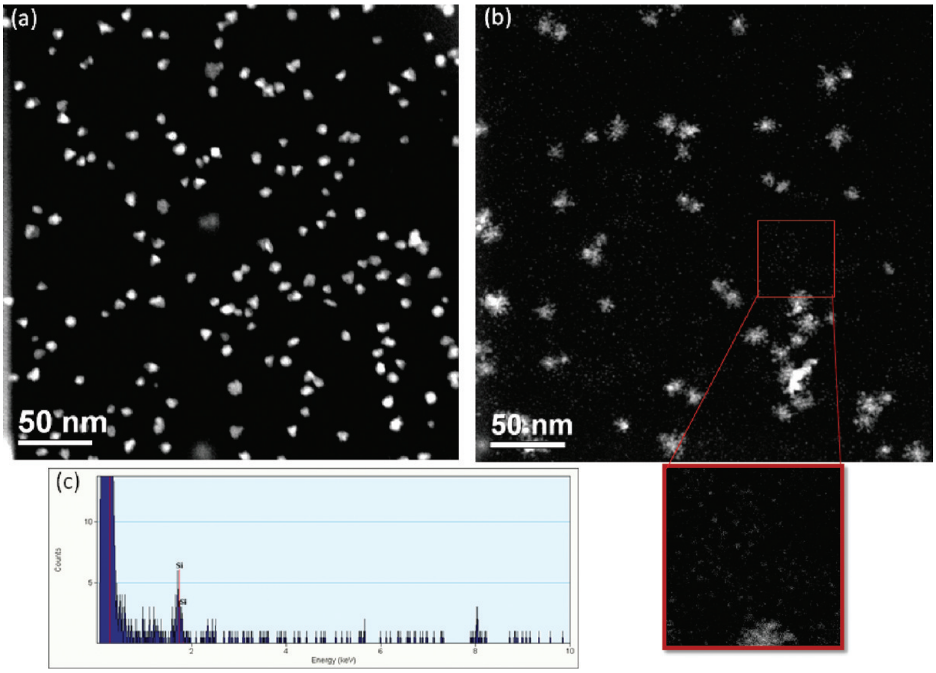

Figure 2. STEM images of (a) GP w/o PEG and (b) GPP1500-60 and (c) EDX analysis of silica nanoparticles.

information, relatively less silica content is observed in GP w/o PEG in Figure 4a than that in GPP1500-60 in Figure 4b by comparing with their theoretical weight percentages, although we cannot calculate the volume fraction from the area fraction directly. The missing silicon-containing components in GP w/o PEG are assigned to unhydrolyzed and monofunctional groups (i.e., A and B in Figure 3c) which are too small to be captured by STEM. Conversely, a considerable portion of much smaller silica particles in GPP1500-60 could be observed in Figures 2b and 4b, although fewer bigger silica particles exist. These tiny nanodots (3.0 nm^2) are located around the agglomerated patterns, and all the particles in GPP1500-60 do not exhibit regular sharp edge as observed in GP w/o PEG. The distance from one dot to another is less than 5 nm, which is in the length range of PPO−PEO−PPO segments of the matrix. These are the strong evidence to prove that the cross-linking in GPP1500-60 involves more structure C and D rather than structure A and B in Figure 3c.

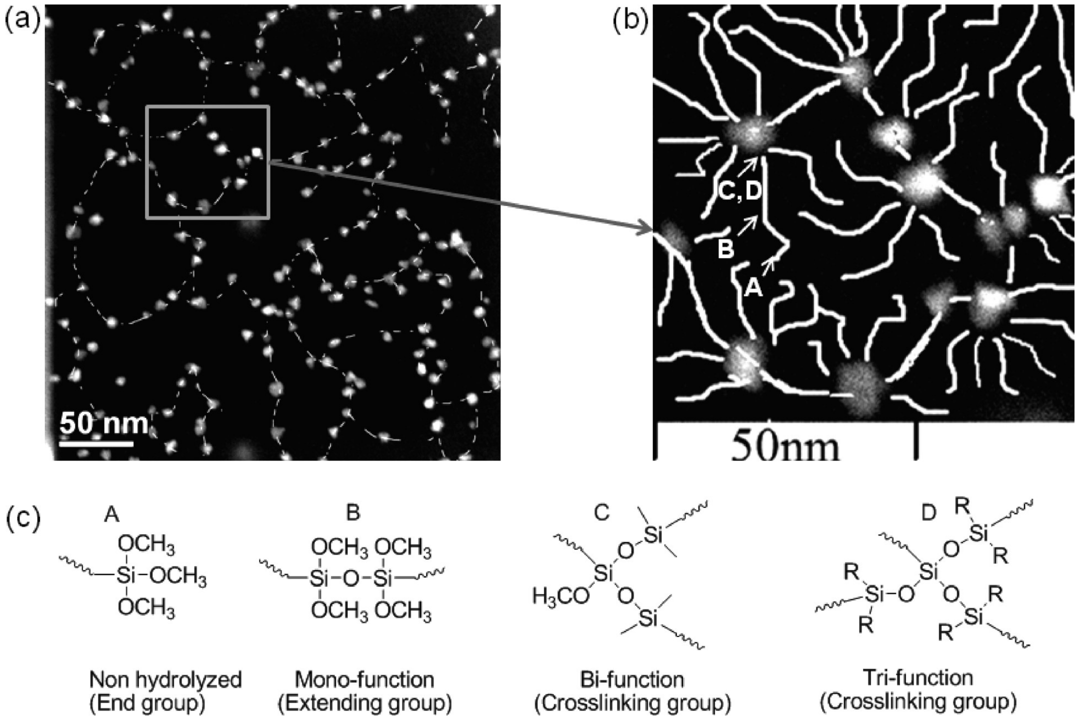

Figure 3. STEM images of (a) hybrid membranes and (b) imaginary matrix constructed with (c) different functional groups.

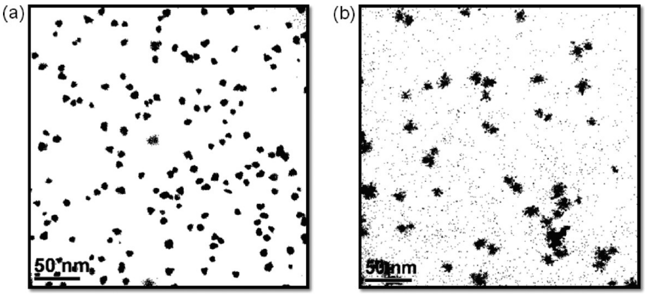

Figure 4. STEM images of hybrid membranes after imageJ analysis: (a) GP w/o PEG and (b) GPP1500-60.

Table 3. Average Size and Area Fraction of Silica Particles in GP w/o PEG and GPP1500-60

	count	average size (nm^2)	area fraction (%)	silica (wt %)
GP w/o PEG	106 ± 4	44 ± 2	7.5 ± 2	11.1
GPP1500-60	1370 ± 70	3.0 ± 0.2	4.7 ± 1	4.4

The hydrophilic PEGs absorb the water released from the condensation reactions. Thus, the reaction equilibrium moves to the product side. In other words, more silica nanoparticles will be formed instead of being individual silicon-containing functional groups. This is also consistent with the result of particle area analyses in Table 3. Strong affinity of PEG with water molecules promotes the condensation reaction and the formation of nanosilica nuclei. Another reason for the morphological difference is that the high viscosity of PEG molecules prevents the growth of nanosilica nuclei from forming bigger particles.

2. XRD Characterization. The smooth broad peak in Figure 5a shows that GP w/o PEG is amorphous at room temperature because freezing at −20 °C cannot induce crystallization as its T_c is at −24.4 °C. GPP400 series are also amorphous because their melting points are below room temperature. GPP1000, GPP1500, and GPP2000 series show two characteristic peaks of PEO in Figure 5b−d. The peak at scattering angle $2\theta = 19.2°$ ($d = 4.62$ Å) corresponds to the reflections from (120) planes of the monoclinic PEG crystal. Another peak at $2\theta = 23.3°$ ($d = 3.81$ Å) contains the overlapped reflections from (032), $(1\bar{3}2)$, (112), $(\bar{2}12)$, $(\bar{1}24)$, $(\bar{2}04)$, and (004) planes.[51]

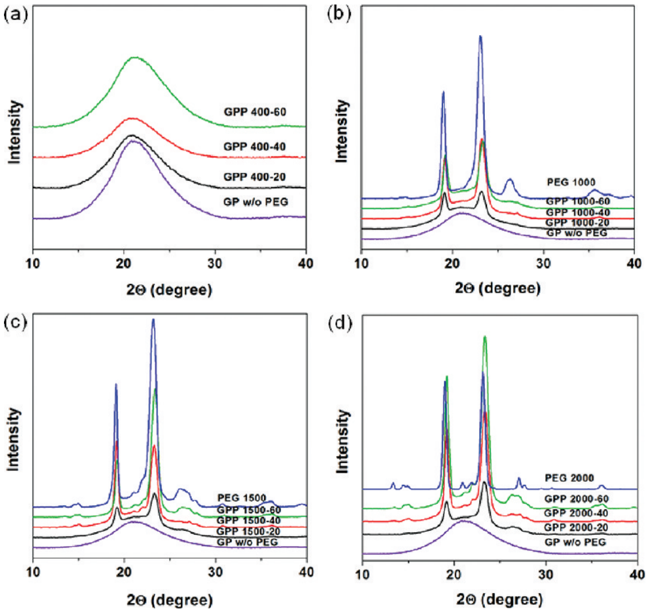

Figure 5. XRD patterns for (a) GPP400, (b) GPP1000, (c) GPP1500, and (d) GPP2000 at room temperature.

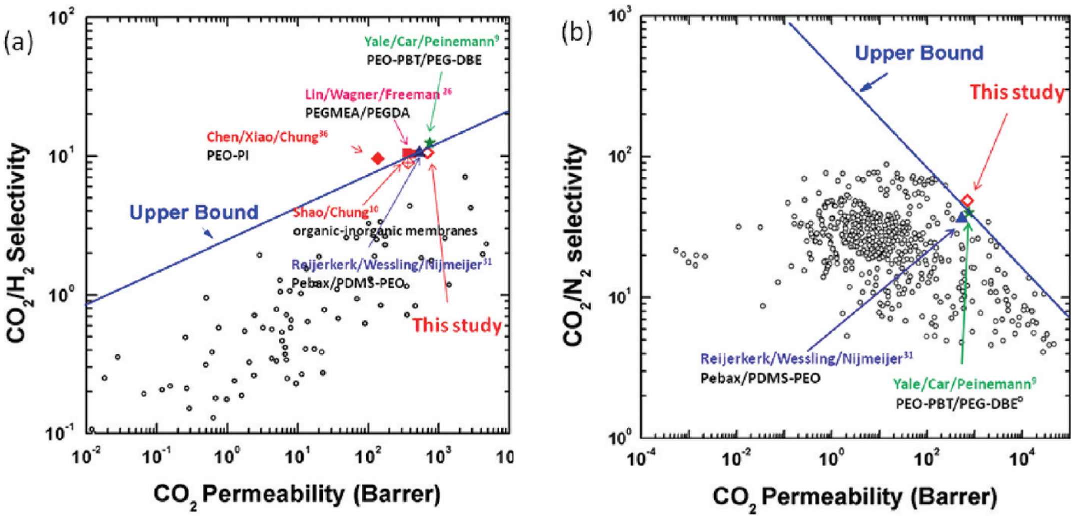

Figure 6. Selected permeability/selectivity data map for (a) CO_2/H_2 and (b) CO_2/N_2 separation at 35 °C.

3. Gas Permeation Performance. CO_2 permeability and CO_2/light gas permselectivity of PEO-based membranes strongly depend on the EO group concentration.[23] Because of the existence of PEG crystals, which are thought to be impermeable, CO_2 permeability and CO_2/light gas permselectivity are compromised. By rising the temperature, CO_2 permeability and CO_2/light gas permselectivity could ramp up because of more available EO groups after melting. In this matrix, the molecular weight of PEGs also plays a key role in determining the performance for the reason for interactions at molecular level. The above factors will be described in more details in the following sections. The best data point with CO_2 permeability of 696 barrer and CO_2/H_2 selectivity at 10.6 at 35 °C almost reach the empirical limit compared to the upper bound[52] as shown in Figure 6a, while the CO_2/N_2 separation performance already exceeds the upper bound[26] as shown in Figure 6b.

The CO_2, H_2, and N_2 permeability of GPP400, -1000, -1500, and -2000 series at different temperatures are depicted in Table 4. For easy comparison, gas permeation performance of GP w/o PEG and pure semicrystalline PEO are also listed in Table 4.

The gas permeation performance of GP w/o PEG is comparable to the previous work.[10] The reason for the higher H_2 and CO_2 permeability compared to the pure semicrystalline PEO is that the crystallinity of PEO segments in GP w/o PEG is greatly suppressed by the cross-linking.

For GPP400 and GPP1000 series, both permeability and permselectivity are improved at 35 and 45 °C, which is contradictory to the trade-off relationship of glassy polymers. These membranes take the advantage of the higher solubility selectivity of CO_2 over H_2 and N_2 introduced by EO groups. As mentioned previously, the EO group concentration determines the CO_2/light gas selectivity. By increasing weight percentage of PEG400, the CO_2/H_2 permselectivity increases from 8.2 (no PEG) to 10.7 (60 wt % PEG400) at 35 °C. The CO_2 permeability increases by more than 50% at 35 °C with 60 wt % of PEG400 in the matrix. The diffusivity increment is the major driving force for the permeability improvement, while the CO_2 solubility shows little change with the addition of PEG400 and PEG1000 as shown in Table 5. The liquid PEGs in the matrix greatly facilitates the transportation of CO_2, leading to an ultrahigh diffusivity than the conventional solid membranes.

Upon surpassing the melting temperatures, GPP1500 and -2000 show tremendous permeability jumps due to significant increments in both diffusivity and solubility as listed in Table 5. Because of the existence of PEG crystals, the permeability of all gases for GPP1500 series is smaller than that for GP w/o PEG at 35 °C. Nevertheless, the CO_2 permeability rises by 10 times after the crystals melt. CO_2 permeability of GPP1500-60 increases from 55.6 barrer at 35 °C to 809 barrer at 45 °C. Within our expectation, the permeability of GPP2000 series is still lower than GP w/o PEG even at 45 °C because PEG crystals do not fully melt. In order to investigate the permeation properties of GPP2000 series in a liquid state, the permeation cell is heated up to 55 °C to facilitate the melting of PEG2000. A similar permeability jump (from 68 barrer at 35 °C to 1040 barrer at 55 °C) is observed. The melting point measured by DSC is slightly higher than that observed from the permeation jumping. This difference could be caused by the temperature lag in the dynamic DSC measurement.

Normally, gas permeability will increase with increasing PEG content. On the contrary, the permeability declines with increasing PEG content when PEG is in a semicrystalline form as shown in Figure 7. The main reason for this phenomenon is that the PEG crystals are considered as impermeable domains for gases. In addition, the shape, size, and size distribution of the crystallites affect the tortuosity and the chain mobility of the amorphous phase. Thus, the diffusivity decreases when the impermeable crystals exist. Furthermore, semicrystalline membranes have lesser sorption sites than amorphous membranes. Sorption measurements reveal that the CO_2 solubility of GPP1500 and GPP2000 is smaller in the semicrystalline state as shown in Table 5. In conclusion, increasing PEG content in the semicrystalline membranes will lead to less amorphous regions and create more complicated tortuosity for gas diffusion. Thus, the permeability decreases because of the lower diffusivity and the lower solubility.

The permselectivity varies a lot when PEG content or temperature changes. For membranes with liquid PEGs, the CO_2/H_2 permselectivity increases in pace with the PEG content as shown in Figure 8 because of the increased EO concentration. For membranes with PEG crystals, the CO_2/H_2 permselectivity decreases with increasing PEG content because the size sieving

Table 4. Pure Gas Permeability and Selectivity for Membranes with Different Compositions at 35, 45, and 55 °C[a]

sample[b]	T (°C)	T_{m2p} (°C)[c]	P_{H2}[d] (barrer)	P_{N2}[d] (barrer)	P_{CO2}[d] (barrer)	CO_2/H_2 selectivity	CO_2/N_2 selectivity
GP w/o PEG	35	14.9	33.4	6.25	275	8.2	44.0
	45		49.2	9.90	344	7.0	34.7
GPP400-20	35	20.5	36.0	7.29	333	9.3	45.7
	45		53.1	11.7	413	7.8	35.3
GPP400-40	35	19.3	37.4	7.54	363	9.7	48.1
	45		53.5	11.9	455	8.5	38.2
GPP400-60	35	20.0	40.0	8.20	427	10.7	52.4
	45		53.8	12.9	479	8.9	37.1
GPP1000-20	35	35.2	41.5	8.40	383	9.2	45.8
	45		61.0	13.4	474	7.8	35.4
GPP1000-40	35	41.7	55.0	11.2	540	9.8	48.2
	45		79.5	18.3	662	8.3	36.2
GPP1000-60	35	45.0	65.9	14.3	696	10.6	48.7
	45		86.6	20.4	845	9.8	41.4
GPP1500-20	35	43.3	25.2	4.30	178	7.1	41.4
	45		67.5	14.4	509	7.5	35.3
GPP1500-40	35	46.8	20.4	3.32	141	6.9	42.5
	45		70.3	16.0	566	8.1	35.4
GPP1500-60	35	48.5	9.30	1.38	55.6	6.0	40.3
	45		96.0	22.3	809	8.4	36.3
GPP2000-20	35	46.2	20.1	3.31	139	6.9	42.0
	45		38.1	8.70	274	7.2	31.4
	55		97.0	22.7	604	6.3	26.6
GPP2000-40	35	52.3	18.0	3.01	128	7.1	42.4
	45		38.9	8.50	285	7.3	33.7
	55		111	23.0	749	6.7	32.6
GPP2000-60	35	54.7	11.5	1.70	68.0	5.9	40.0
	45		25.8	4.73	163	6.3	34.5
	55		143	34.1	1040	7.3	30.5
semicrystalline PEO[28]	35	68.0	1.8	0.24	13	7.2	54
	45		6.4	0.99	40	6.3	40

[a] 55 °C was only employed for GPP2000 series. [b] GPP*X*-*Y* represents the sample code, where *X* is the molecular weight and *Y* is the weight percentage of PEG blended. [c] Peak melting temperatures of the second heating curve. [d] Permeability, 1 barrer = 10^{-10} cm^3 (STP) cm/(cm^2 s cmHg).

effect is enhanced by the increasing tortuosity. In rubbery materials, permselectivity usually weights heavier on solubility selectivity. Although H_2 diffuses faster than CO_2, the permeability of CO_2 is still much larger than H_2 because of the higher solubility. Diffusivity selectivity of CO_2/H_2 is usually less than 1 due to the size sieving effect. However, the CO_2 diffusivity gains a lot upon traversing the melting point, leading to a relative smaller diffusivity difference between CO_2 and H_2. Thus, the overall selectivity is improved by minimizing the size sieving effect with the aid of across the melting point. As shown in Figure 8, the CO_2/H_2 permselectivity of GPP1500 series after PEG crystals melting is improved to different extents depending on the PEG content in the blends. GPP1500 with 60 wt % PEG shows the greatest improvement from 6.0 to 8.4, while GPP2000 series show less CO_2/H_2 permselectivity improvement because PEG2000 crystals only partially melt as indicated by the small melting peaks at lower temperatures in Figure 9d.

Table 6 shows the CO_2/N_2 mixed gas results. A considerable CO_2/N_2 selectivity decrease from 41.4 to 31.3 for GPP1000-60 and from 36.3 to 32.0 for GPP1500-60 at 45 °C is observed. CO_2 permeability is comparable with the pure gas permeability for both samples. However, the N_2 permeability increases from 20.4 to 26.8 barrer for GPP1000-60 and from 22.3 to 26.2 barrer for 1500-60. These phenomena are probably caused by the CO_2 plasticization in the solubility selectivity membranes.[53]

4. Effect of Testing Temperature. The effect of testing temperature on CO_2 permeability of GPP1500-60 is illustrated in Figure 10. The CO_2 permeability increases from 26 barrer at 30 °C to 860 barrer at 55 °C. The temperature dependence of permeability without thermal transition could be described by Arrhenius expression $P = P_0 \exp(-E_p/RT)$. These linear relationships are only observed at lower temperatures and higher temperatures. In between these two regions, a jump of permeability is observed near the onset melting temperature as shown in Figure 10. Mogri and Paul[54,55] have also observed a change in permeability of 2 orders of magnitude when the side chains of poly(octadecyl acrylate) melt. Hirayama et al.[33] and Kim et al.[56] have also observed an abrupt increase of permeability when PEG melt in their PEG-based materials. Nonlinear relationships appear with the thermal transition because E_p is changed as well as the three parameters shown in eq 9. The decrease of the activation energy for diffusion could be caused by the change of diffusion mechanism from the hopping diffusion to the liquidlike diffusion.[49] The diffusivity of gases in the polymer melt could

Table 5. Gas Permeability, Solubility, and Diffusivity Coefficient Results Compared with PDMS and PEO from Other Sources

	P_{CO_2}[b] (barrer)		S_{CO_2} (cm^3 STP/(cm^3 atm))		$D_{CO_2} \times 10^6$ (cm^2/s)	
samples[a]	35 °C	45 °C	35 °C	45 °C	35 °C	45 °C
GP w/o PEG	275	344	1.59	1.16	1.32	2.26
GPP400-20	333	413	1.47	1.15	1.72	2.73
GPP400-40	363	455	1.48	1.25	1.87	3.00
GPP400-60	427	479	1.50	1.19	2.17	3.05
GPP1000-20	387	474	1.51	1.17	1.93	3.07
GPP1000-40	540	662	1.65	1.27	2.48	3.97
GPP1000-60	696	845	1.65	1.25	3.20	5.14
GPP1500-20	178	509	1.14	1.24	1.19	3.12
GPP1500-40	141	566	0.82	1.27	1.31	3.39
GPP1500-60	55.6	810	0.54	1.31	0.78	4.68
GPP2000-20	139	274	0.99	1.19	1.07	1.76
GPP2000-40	128	285	0.74	1.22	1.32	1.77
GPP2000-60	68	163	0.46	1.29	1.13	0.96
semicrystalline PEO[28]	13	40	0.37	N/A	0.27	N/A
amorphous PEO-35[28]	143	N/A	1.3	N/A	0.86	N/A
PDMS-35[25]	3800	N/A	1.3	N/A	22.2	N/A

[a] GP*X*-*Y* represents the sample code, where *X* is the molecular weight and *Y* is the weight percentage of PEG blended. [b] 1 barrer = 10^{-10} cm^3 (STP) cm/(cm^2 s cmHg).

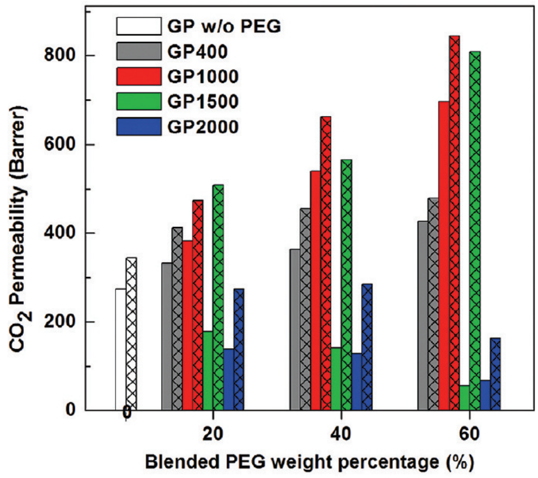

Figure 7. CO$_2$ permeability of GPP series and GP w/o PEG at 35 °C (blank) and 45 °C (checked).

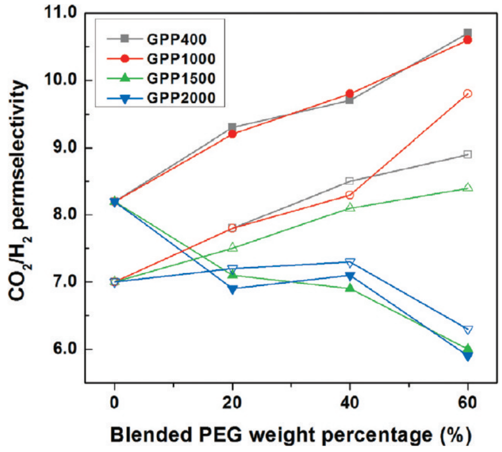

Figure 8. Permselectivity at 35 °C (solid) and 45 °C (hollow) for CO$_2$/H$_2$.

reach the diffusive limit on a time scale similar to that of the polymer melt. Meanwhile, the tortuosity will be minimized, and the chain motion in the amorphous region will be no longer affected by the crystallites. There is a 6 times increment in diffusivity of GPP1500-60 at 45 °C than that at 35 °C as shown in Table 5. The absolute value of condensation enthalpy will not change because it is determined by the penetrants themselves. However, the mixing enthalpy of CO$_2$- and PEO-based polymers will be more negative because less energy is needed to allow CO$_2$ molecules penetrate into the matrix. Thus, the solubility increases when a thermal transition happens. Afterward, the solubility will decrease when the temperature further increases.

The solid lines in Figure 11a,b represent the CO$_2$ sorption isotherms and the solubility coefficients of GPP1500 series and GP w/o PEG at 35 °C, while the dashed lines represent the sorption at 45 °C. The solubility coefficients increase from 0.54, 0.82, and 1.14 to 1.31, 1.27, and 1.24 cm^3 (STP)/(cm^3 atm) for GPP1500-60, GPP1500-40, and GPP1500-20 after melting, respectively. Being the membrane with the highest crystal content, GPP1500-60 shows the lowest solubility coefficient close to that of the semicrystalline PEO at 35 °C, as shown in Figure 12b. On the contrary, the solubility coefficient of GP w/o PEG decreases from 1.59 to 1.16 cm^3 (STP)/(cm^3 atm) when temperature increases because there is no thermal transition. For the same reason, GPP1000 series which PEG1000 crystals already melt at both temperatures shows a solubility loss as shown in Table 5. However, the diffusivity increment overweighs the slight decrease of solubility. Therefore, the permeability still shows considerable enhancement at 45 °C. CO$_2$ permeability of GPP1000-60 increases from 696 to 845 barrer despite its solubility decreases from 1.65 to 1.25 cm^3 (STP)/(cm^3 atm). The solubility

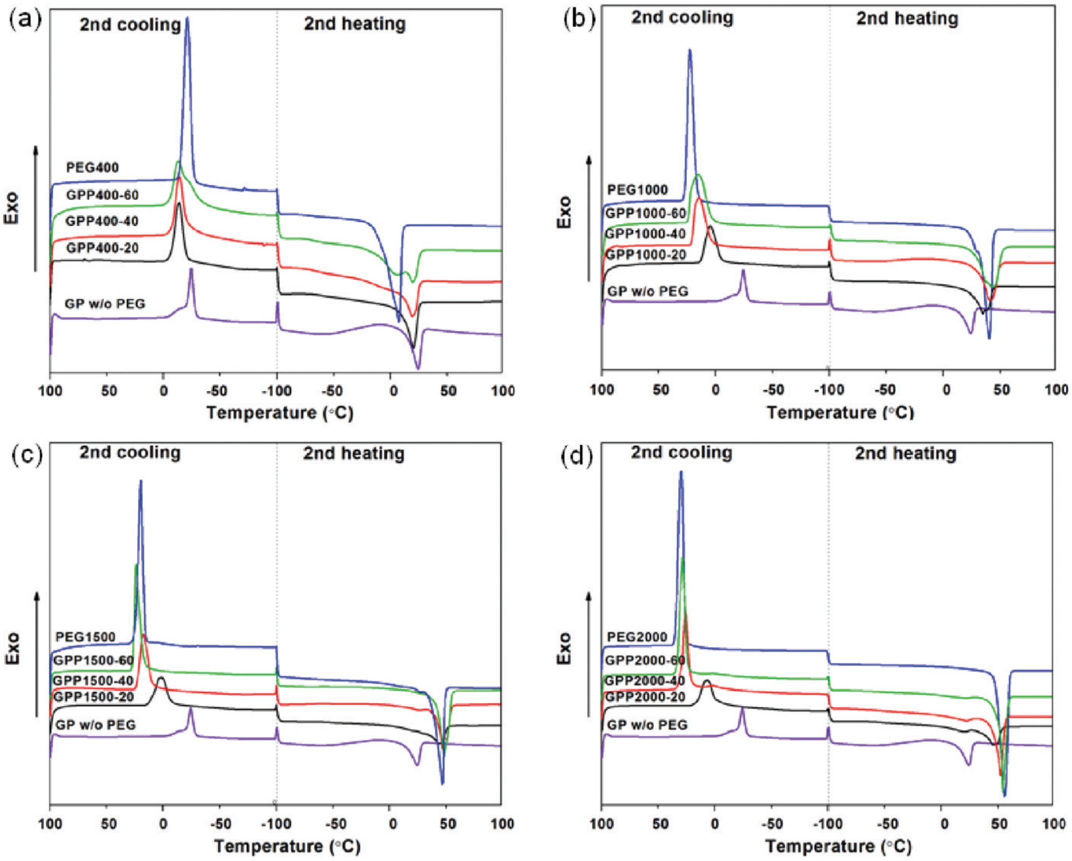

Figure 9. DSC curves for (a) GPP400, (b) GPP1000, (c) GPP1500, and (d) GPP2000.

Table 6. Mixed Gas Permeability and Selectivity for GPP1000-60 and GPP1500-60 at 45 °C

	50:50 CO_2/N_2 mixed gas		
sample	P_{CO2} (barrer)	P_{N2} (barrer)	CO_2/N_2 selectivity
GPP1000-60	839 (845)[a]	26.8 (20.4)	31.3 ± 0.6 (41.4)
GPP1500-60	838 (809)	26.2 (22.3)	32.0 ± 0.5 (36.3)

[a] Number in parentheses is the permeability and permselectivity tested by pure gases.

of GPP1000 series at 35 °C could reach 1.5−1.6 cm^3 STP/(cm^3 atm), which is comparable with the solubility of amorphous PEO[28] (1.3 cm^3 STP/(cm^3 atm)) as shown in Figure 12b and the cross-linked PEO rubber[15] (1.5 cm^3 STP/(cm^3 atm)). The solubility of GPP2000 series increases from 0.46−0.99 to 1.19−1.29 cm^3 (STP)/(cm^3 atm) due to the partial melting as indicated by the small melting peaks as shown in Figure 9d.

5. Effect of PEGs' Molecular Weights. Figure 13 shows the solubility and diffusivity of blend membranes containing 40 wt % PEGs at 45 °C. The CO_2 solubility for these membranes varies little as they have the same PEG content, while the CO_2 permeability changes dramatically. GPP1000-40 has the highest diffusivity while GPP2000-40 is the lowest. For other samples with different contents of PEGs, the trend is almost the same. The lowest diffusivity of GPP2000-40 can be ascribed to the partial melting of the PEG crystals. However, the diffusivity difference among GPP400-40, GPP1000-40, and GPP1500-40 could only be ascribed to the molecular weight difference because these PEGs are already in liquid states. Because of the technical limitation, there is no suitable characterization method available to monitor the effect of molecular weight on diffusivity

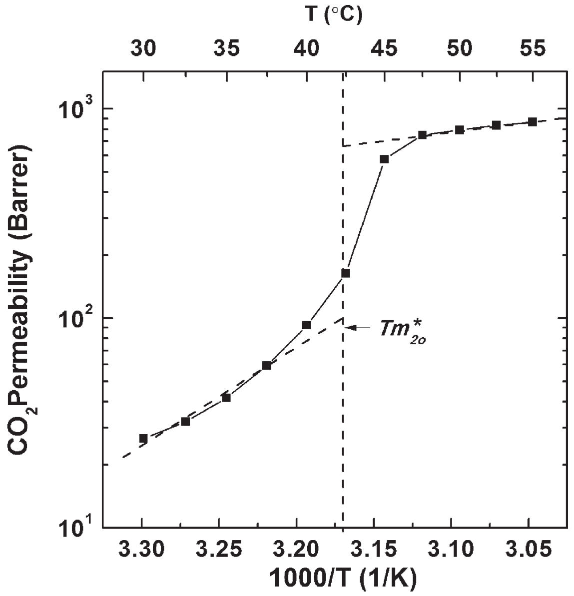

Figure 10. Change of CO_2 permeability of GPP1500-60 from 30 to 55 °C. T^*_{m2o} is the onset melting temperature of PEG1500 in GPP1500-60 during second heating.

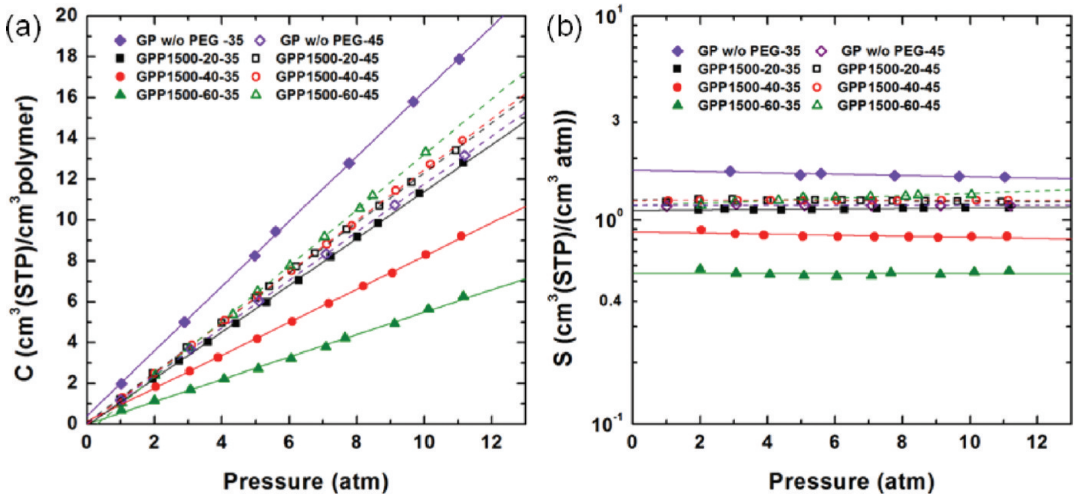

Figure 11. CO_2 sorption isotherm (a) and solubility coefficient (b) of GPP1500 at 35 and 45 °C.

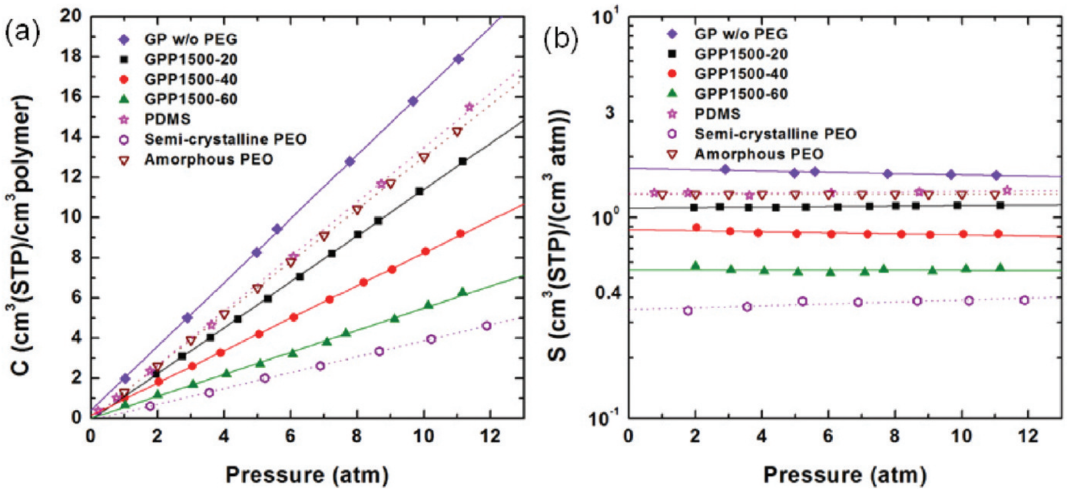

Figure 12. Sorption isotherm (a) and solubility (b) of GPP1500, PDMS,[25] semicrystalline PEO, and amorphous PEO[28] at 35 °C.

coefficient above the melting temperature. An alternative method by analyzing the crystallization and melting behavior of the blend membranes becomes an important way to understand this phenomenon. Although melting is observed from DSC, we could still assume that liquid PEG molecules in the matrix only vibrate violently in the confined environment rather than free-flowing. Extensive studies have been done in the past decades to understand the crystallization behavior of low molar mass PEGs. It is well-known that PEG with a low molecular weight ($M_w \leq 3000$ g/mol) crystallizes exclusively with extended chains under normal cooling rate.[57,58] In this scenario, we propose a possible crystallization mechanism as depicted in Figure 14. PEGs with different molecular weights will have different orientations and alignments in the confined environment. During membrane fabrication, PEGs are heated to 70 °C to surpass their melting temperatures so that the equilibrium could be reached between the PEO segments of the matrix and the liquid PEG molecules. The compatibility between the PEO segments and the PEG molecules is fairly good so that they crystallize together upon cooling. All the membranes present one crystallization peak during second cooling, although some of the membranes have two melting peaks as shown in Figure 8a–d. Analysis on the heat of crystallization in Table 2 also supports the assumption of cocrystallization. ΔH_c is the heat of crystallization obtained experimentally from the integration of DSC peak area. $\Delta H_c'$ is the theoretical value calculated from

$$\Delta H_c\prime = \Delta H_c(\text{PEG}) \times \text{wt }\%(\text{PEG}) + \Delta H_c(\text{matrix}) \times (1 - \text{wt }\%(\text{PEG})) \qquad (11)$$

ΔH_c and $\Delta H_c'$ values of GPP1000, -1500, and -2000 series are almost the same. For the GPP400 series, ΔH_c is smaller than $\Delta H'_c$, revealing that the GPP400 series is easier to crystallize. Crystallization temperatures of GPP400 blends, which are higher than both GP w/o PEG and PEG400, also provide strong evidence for the conclusion that GPP400 series has the strongest interactions with the PEO segments in the matrix. Thus, the diffusivity of GPP400 series should be the lowest due to its highest tendency to crystallize. This correlates well with the result obtained from sorption experiments. High concentration of hydrogen bonding of PEG400 may be the reason for their strong crystallization tendency.

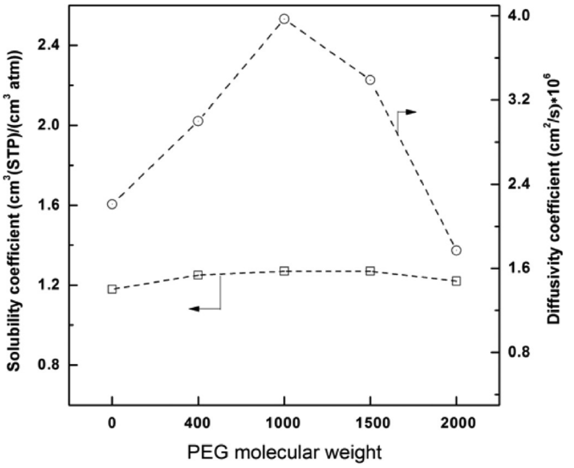

Figure 13. Solubility (square) and diffusivity (circle) of hybrid membranes containing 40 wt % of PEG with different molecular weights at 45 °C.

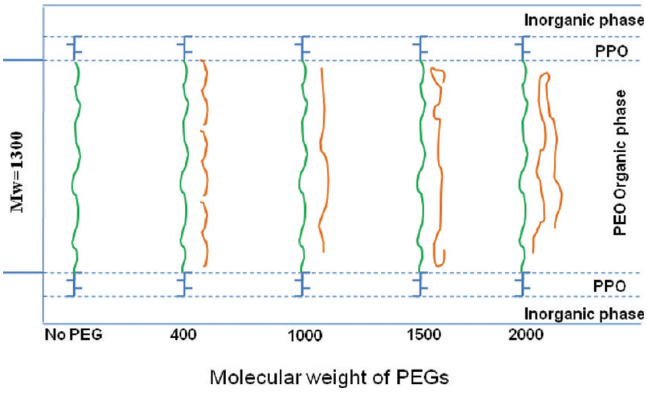

Figure 14. Crystallization of PEO segments and PEGs with different molecular weights.

In GP w/o PEG, PEO segments cannot fully crystallize due to the cross-linking. A shoulder peak rather than a symmetric exothermic peak in the cooling curve is observed, indicating that a considerable amount of imperfect PEO crystals are formed because of the confinement. The crystallization peaks of GPP1000, -1500, and -2000 are located in between the peaks of the GP w/o PEG and the respective pure PEGs. The fully extended PEG chains may facilitate the PEO segments of the matrix to crystallize by reducing the extra free energy required to align chain segments. Thus, the crystallization temperature increases with PEG content.

Crystal defects and lots of chain ends are created during crystallization because of different chain lengths as illustrated in Figure 14. Several PEG400 molecules could be aligned along one PEO segment ($M_w \approx 1300$). However, only one PEG1000 chain is allowed to align along the PEO segment because of their similar molecular weights and chain lengths. Once one PEG1000 chain is aligned with the PEO segment, the remaining portion of the PEO segment may not arrange regularly, thus leading to more defects. Therefore, the diffusivity of GPP1000 series is the highest. The PEO segments of the matrix could be fully coupled with PEG1500 because of their similar chain lengths. One folding may exist when PEG2000 is employed because its chain length almost doubles that of the PEO segment. The diffusivity of GPP1500 is slightly lower than that of GPP1000 at 45 °C because fewer defects are created.

■ CONCLUSIONS

This paper introduces a novel method of employing liquid PEG as a gas separation medium. The PEO−silica organic−inorganic network synthesized by the sol−gel process has been proved to be an effective matrix for holding liquid PEG. The permeability has been improved more than twice without losing permselectivity when PEG with a proper molecular weight is employed. With the loading of PEG molecules, CO_2/H_2 and CO_2/N_2 permselectivity is found to increase by more than 10%. A significant permeability jump is observed when the testing temperature surpasses the melting point of PEG. Diffusivity increment is considered as the major contributor to the permeability jump, while the solubility shows little change if there is no thermal transition. A considerable increase of solubility coefficient is observed when solid PEG becomes liquid. Four PEGs with different molecular weights have been investigated. PEG1000, which has a similar molecular weight to the PEO segments in the PEO−silica organic−inorganic matrix, is proved to be the best candidate to improve both CO_2 permeability and CO_2/light gas permselectivity.

Great potential for commercialization is observed on these materials. However, PEO-based materials are usually difficult to be fabricated into hollow fibers or asymmetric membranes due to their hydrophilicity and low mechanical strength. Thus, multilayer thin film composite membranes[59,60] seem to be the best candidate for the large-scale CO_2 capture. Continuous coating of these materials on a hollow fiber substrate is ongoing in our group. Long-term stability studies under real operating conditions are also needed in the future.

■ ACKNOWLEDGMENT

The authors express their gratitude to NUS and A*Star for funding this work with the grants of R-398-000-044-305 (NUS) and 092 139 0033 (A-Star) as well as the Singapore National Research Foundation (NRF) for the support on the project entitled “Molecular Engineering of Membrane Materials: Research and Technology for Energy Development of Hydrogen, Natural Gas and Syngas” with Grant R-279-000-261-281. The authors also thank Prof. D. R. Paul (University of Texas, Austin), Prof. Hong Liang, Dr. Lin Ming, Dr. Xiao Youchang, Ms. Wang Honglei, and other colleagues in our group for their valuable discussions and help.

■ REFERENCES

(1) Kintisch, E.; Regalado, A. *Science* **2010**, *330*, 1597–1597.

(2) Schrag, D. P. *Science* **2007**, *315*, 812–813.

(3) Sims, R. E. H.; Rogner, H. H.; Gregory, K. *Energy Policy* **2003**, *31*, 1315–1326.

(4) Damen, K.; van Troost, M.; Faaij, A.; Turkenburg, W. *Prog. Energy Combust. Sci.* **2006**, *32*, 215–246.

(5) Merkel, T. C.; Lin, H.; Wei, X.; Baker, R. *J. Membr. Sci.* **2010**, *359*, 126–139.

(6) Rochelle, G. T. *Science* **2009**, *325*, 1652–1654.

(7) Yang, S. I.; Choi, D. Y.; Jang, S. C.; Kim, S. H.; Choi, D. K. *Adsorption* **2008**, *14*, 583–590.

(8) Yave, W.; Car, A.; Peinemann, K. V.; Shaikh, M. Q.; Rätzke, K.; Faupel, F. *J. Membr. Sci.* **2009**, *339*, 177–183.

(9) Yave, W.; Car, A.; Funari, S. S.; Nunes, S. P.; Peinemann, K. V. *Macromolecules* **2010**, *43*, 326–333.

(10) Shao, L.; Chung, T. S. *Int. J. Hydrogen Energy* **2009**, *34*, 6492–6504.

(11) Patel, N. P.; Zielinski, J. M.; Samseth, J.; Spontak, R. J. *Macromol. Chem. Phys.* **2004**, *205*, 2409–2419.

(12) Patel, N. *Polymer* **2004**, *45*, 5941–5950.

(13) O'Brien, K. C.; Krishnan, G.; Berchtold, K. A.; Blum, S.; Callahan, R.; Johnson, W.; Roberts, D.-L.; Steele, D.; Byard, D.; Figueroa, J. *Energy Procedia* **2009**, *1*, 287–294.

(14) Munoz, D.; Maya, E.; Deabajo, J.; Delacampa, J.; Lozano, A. *J. Membr. Sci.* **2008**, *323*, 53–59.

(15) Lin, H.; Wagner, E. V.; Swinnea, J. S.; Freeman, B. D.; Pas, S. J.; Hill, A. J.; Kalakkunnath, S.; Kalika, D. S. *J. Membr. Sci.* **2006**, *276*, 145–161.

(16) Husken, D.; Visser, T.; Wessling, M.; Gaymans, R. J. *J. Membr. Sci.* **2010**, *346*, 194–201.

(17) Brunetti, A.; Scura, F.; Barbieri, G.; Drioli, E. *J. Membr. Sci.* **2010**, *359*, 115–125.

(18) Xiao, Y. C.; Chung, T. S. *Energy Environ. Sci.* **2011**, *4*, 201–208.

(19) Low, B. T.; Xiao, Y.; Chung, T. S. *Polymer* **2009**, *50*, 3250–3258.

(20) Shao, L.; Chung, T. S.; Goh, S.; Pramoda, K. *J. Membr. Sci.* **2005**, *256*, 46–56.

(21) Tin, P. S.; Chung, T. S.; Liu, Y.; Wang, R.; Liu, S. L.; Pramoda, K. P. *J. Membr. Sci.* **2003**, *225*, 77–90.

(22) Xia, J.; Liu, S.; Pallathadka, P. K.; Chng, M. L.; Chung, T. S. *Ind. Eng. Chem. Res.* **2010**, *49*, 12014–12021.

(23) Lin, H.; Freeman, B. D. *J. Mol. Struct.* **2005**, *739*, 57–74.

(24) Pinnau, I.; He, Z. *J. Membr. Sci.* **2004**, *244*, 227–233.

(25) Merkel, T. C.; Bondar, V. I.; Nagai, K.; Freeman, B. D.; Pinnau, I. *J. Polym. Sci., Part B: Polym. Phys.* **2000**, *38*, 415–434.

(26) Lin, H.; Van Wagner, E.; Freeman, B. D.; Toy, L. G.; Gupta, R. P. *Science* **2006**, *311*, 639–642.

(27) Lin, H.; Freeman, B. D.; Kalakkunnath, S.; Kalika, D. S. *J. Membr. Sci.* **2007**, *291*, 131–139.

(28) Lin, H.; Freeman, B. D. *J. Membr. Sci.* **2004**, *239*, 105–117.

(29) Zhao, H. Y.; Cao, Y. M.; Ding, X. L.; Zhou, M. Q.; Liu, J. H.; Yuan, Q. *J. Membr. Sci.* **2008**, *320*, 179–184.

(30) Yave, W.; Car, A.; Peinemann, K. V. *J. Membr. Sci.* **2010**, *350*, 124–129.

(31) Reijerkerk, S. R.; Knoef, M. H.; Nijmeijer, K.; Wessling, M. *J. Membr. Sci.* **2010**, *352*, 126–135.

(32) Kusuma, V. A.; Freeman, B. D.; Borns, M. A.; Kalika, D. S. *J. Membr. Sci.* **2009**, *327*, 195–207.

(33) Hirayama, Y.; Kase, Y.; Tanihara, N.; Sumiyama, Y.; Kusuki, Y.; Haraya, K. *J. Membr. Sci.* **1999**, *160*, 87–99.

(34) Car, A.; Stropnik, C.; Yave, W.; Peinemann, K. V. *J. Membr. Sci.* **2008**, *307*, 88–95.

(35) Li, Y.; Chung, T. S. *Int. J. Hydrogen Energy* **2010**, 35, 10560–10568.

(36) Chen, H.; Xiao, Y.; Chung, T. S. *Polymer* **2010**, *51*, 4077–4086.

(37) Car, A.; Stropnik, C.; Yave, W.; Peinemann, K. V. *Adv. Funct. Mater.* **2008**, *18*, 2815–2823.

(38) Car, A.; Stropnik, C.; Yave, W.; Peinemann, K. V. *Sep. Purif. Technol.* **2008**, *62*, 110–117.

(39) Husken, D.; Feijen, J.; Gaymans, R. J. *J. Polym. Sci., Part A: Polym. Chem.* **2007**, *45*, 4522–4535.

(40) Kawakami, M.; Iwanaga, H.; Hara, Y.; Iwamoto, M.; Kagawa, S. *J. Appl. Polym. Sci.* **1982**, *27*, 2387–2393.

(41) Raharjo, R. D.; Lin, H. Q.; Sanders, D. E.; Freeman, B. D.; Kalakkunnath, S.; Kalika, D. S. *J. Membr. Sci.* **2006**, *283*, 253–265.

(42) Kusuma, V. A.; Matteucci, S.; Freeman, B. D.; Danquah, M. K.; Kalika, D. S. *J. Membr. Sci.* **2009**, *341*, 84–95.

(43) Kang, G.; Cao, Y.; Zhao, H.; Yuan, Q. *J. Membr. Sci.* **2008**, *318*, 227–232.

(44) Kalakkunnath, S.; Kalika, D. S.; Lin, H.; Raharjo, R. D.; Freeman, B. D. *Polymer* **2007**, *48*, 579–589.

(45) Kim, T. H.; Koros, W. J.; Husk, G. R. *J. Membr. Sci.* **1989**, *46*, 43–56.

(46) Koros, W. J.; Madden, W. C. *Transport Properties*; John Wiley & Sons, Inc.: New York, 2002.

(47) Lin, W. H.; Vora, R. H.; Chung, T. S. *J. Polym. Sci., Polym. Phys.* **2000**, *38*, 2703–2713.

(48) Li, F.; Li, Y.; Chung, T. S.; Kawi, S. *J. Membr. Sci.* **2010**, *356*, 14–21.

(49) Chung, T. S.; Chan, S. S.; Wang, R.; Lu, Z.; He, C. *J. Membr. Sci.* **2003**, *211*, 91–99.

(50) Abramoff, M. D.; Magelhaes, P. J.; Ram, S. J. *Biophotonics Int.* **2004**, *11*, 36–42.

(51) Wang, H.; Keum, J. K.; Hiltner, A.; Baer, E. *Macromol. Rapid Commun.* **2010**, *31*, 356–361.

(52) Robeson, L. M. *J. Membr. Sci.* **2008**, *320*, 390–400.

(53) Reijerkerk, S. R.; Nijmeijer, K.; Ribeiro, C. P., Jr; Freeman, B. D.; Wessling, M. *J. Membr. Sci.* **2011**, *367*, 33–44.

(54) Mogri, Z.; Paul, D. R. *Polymer* **2001**, *42*, 2531–2542.

(55) Mogri, Z.; Paul, D. R. *J. Membr. Sci.* **2000**, *175*, 253–265.

(56) Kim, J. H.; Ha, S. Y.; Lee, Y. M. *J. Membr. Sci.* **2001**, *190*, 179–193.

(57) Pfefferkorn, D.; Kyeremateng, S. O.; Busse, K.; Kammer, H.-W.; Thurn-Albrecht, T.; Kressler, J. R. *Macromolecules* **2011**, *44*, 2953–2963.

(58) Godovsky, Y. K.; Slonimsky, G. L.; Garbar, N. M. *J. Polym. Sci., Part B: Polym. Symp.* **1972**, *38*, 1–21.

(59) Chung, T. S.; Kafchinski, E. R.; Foley, P.; Kohn, R. S.; Straff, R. S. *J. Appl. Polym. Sci.* **1994**, *53*, 701–708.

(60) Shieh, J. J.; Chung, T. S.; Paul, D. R. *Chem. Eng. Sci.* **1999**, *54*, 675–684.